On the form drag coefficient under ridged ice: Laboratory experiments and numerical simulation from ideal scaling to real ice conditions

Y. Zu[1], P. Lu[1], M. Leppäranta[2], B. Cheng[3], Z. Li[1]

[1]State Key Laboratory of Costal and Offshore Engineering, Dalian University of Technology, Dalian, China.

[2]Institute of Atmosphere and Earth Sciences, University of Helsinki, Helsinki, Finland.

[3]Finnish Meteorological Institute, Helsinki, Finland.

Corresponding author: Peng Lu (lupeng@dlut.edu.cn)

Key Points:

- Parameterization of the form drag coefficient C_d under ridged ice is performed by laboratory experiments and idealized numerical simulation.
- In laboratory experiments with a given water depth, C_d is sensitive to the ridge keel depth and slope angle for the turbulent regime.
- In oceanic conditions of mixed layer much deeper than keel depth, C_d is a logarithmic function of the slope angle α: $C_d=0.68\ln(\alpha/7.8)$.

Abstract

The bottom topography of ridged sea ice differs largely from that of other sea ice types. The form drag on ridge keels plays an important role affecting sea ice drift and deformation. We have carried out laboratory experiments and numerical simulations for a ridge model in a flume in order to better understand the characteristics of the form drag. The experimental setup covered both laminar and turbulent conditions. The local form drag coefficient of a keel, C_d, varied with the keel depth h and slope angle α in the turbulent regime. The numerical model extended the experimental results to independence of the water depth in order to achieve an analogy for ocean conditions. The results showed $C_d = 0.68\ln(\alpha/7.8)$, $R^2 = 0.998$, $10^\circ \leq \alpha \leq 90^\circ$, C_d ranging from 0.14 to 1.66, when keel depth is much smaller than mixed layer depth. In the Arctic Ocean, keel slope angles are within the range of 10˚–50˚ where C_d increases monotonously and becomes the dominant part of the total ice-water drag coefficient when $\alpha \geq 20^\circ$. When h/L_r (the ratio of keel depth to spacing) was high (h/L_r>0.01), the ratio of air-ice to ice-water drag coefficient first decreased and then increased with α and reached the minimum at $\alpha \approx 30^\circ$. The variation of C_d with α (10˚–50˚) affects the momentum transfer of drifting sea ice, and we suggest that C_d under ridged sea ice to be tuned to 0.14–1.26 in multi-category sea ice models.

Plain Language Summary

Drag force on sea ice exerted by air and ocean play a key role in the dynamics of sea ice. Drag force is closely related with the morphology of sea ice. The thinning of

Arctic sea ice may largely affect drag force, because thinner sea ice may be more easily subjected to deformation, resulting in sea ice ridging or hummock ice and further enhancing the dominance of ridge form drag in the total drag force. The drag coefficient is parameterized with the thickness, concentration and floe size in sea ice models. However, the slope angle of the ridge keel, which determines the shape of ridges, also has an important influence on the drag. The local form drag coefficient of ridge was investigated in this study by laboratory experiments and numerical simulations with an ice ridge model. A logarithmic function was found to describe the relationship between the local drag coefficient and the slope angle of keel in conditions of deep mixed layer in the Arctic Ocean. The function of the local form drag coefficient can be directly applied to the current sea ice dynamics models.

1 Introduction

Arctic sea ice has been changing rapidly with global warming in the past several decades (Onarheim et al., 2018). Recent studies have indicated that Arctic sea ice is not only thinning but also shrinking in size (Rothrock et al.,1999; Comiso, 2011; Stroeve et al., 2012). Therefore, the exchange of momentum between the atmosphere and the ocean will be modified with the decline in Arctic sea ice (Martin et al., 2016). A thinner ice cover is easier broken under the actions of ocean waves and wind stress (Castellani et al., 2014; Petty et al., 2017). As a consequence, the drift speed of Arctic pack ice has increased significantly, although the wind force has remained at a similar magnitude to previously (Spreen et al., 2011). In some regions exposed to storm

events, the sea ice distribution can change quickly and the drift speed has even reached 1 m/s (Itkin et al., 2017). Thinner sea ice may be more easily subject to deformation, resulting in sea ice ridging or hummock ice (Lepparänta, 2011). The drift pattern of ridged ice differs considerably from level ice owing to its complicated topography involving a ridge sail in the air and its morphology of ridge keel in the water.

Both of these factors affect sea ice drag force. The drag force depends on the ice surface and bottom roughness, and atmospheric and oceanic boundary-layer flows are the key variables that determine the momentum exchange at the air-ice and ice-ocean interfaces. Early methods of calculating the momentum fluxes mostly regarded the drag coefficients as constants in neutral atmospheric or oceanic boundary layers based on the Monin-Obukhov and Rossby similarity theory (Blackadar and Tennekes, 1968; Obukhov, 1971; Banke et al., 1980). More generally, the drag coefficients depend on the stability of the boundary layer stratification and the roughness length of the sea ice surface and bottom. The turbulent flow regime in the boundary layers was the main consideration in earlier studies (Overland, 1985; McPhee, 2012).

The drag force consists of tangential shear stress or skin friction and the form drag, the drag force component that is normal in large roughness elements, and is exerted on floe edges and ridges by winds and currents (Mai et al., 1996; Garbrecht et al., 2002; Lüpkes et al., 2012). With the decline of multiyear ice (MYI) in the Arctic

Ocean, a thinner ice cover is more easily broken, and the variations in the surface topography are higher than previously (Castellani et al., 2014). Both the air-ice and ice-ocean drag coefficients, C_a and C_w, reach their maximums in the summer during their annual cycle, and contributions from the form drag are significant because the floe size and ridge spacing are reduced more dramatically than the ice thickness during the melt season (Tsamados et al., 2014).

The force exerted on ice ridges is associated with the velocity profiles of the wind/current at different ridge thicknesses, and the local form drag coefficient of an individual obstacle (referred to as the local form drag coefficient, C_d for a keel, C_d' for a sail, the superscript ′ representing air-ice parameters hereinafter) uses a quadratic drag law (Arya, 1973). With the increasing spatial resolutions of the present numerical models, different types of ice floes have been taken into account in multi-category sea ice models that reflect thickness distribution, especially the ridged ice contribution, and the scheme by Arya is widely adopted in present models; for instance, the Helsinki multicategory sea ice model (HELMI) (Haapala et al., 2005; Mårtensson et al., 2012) and the Los Alamos sea ice model (CICE) (Hunke et al., 2013; Tsamados et al., 2014; Martin et al., 2016). The results from using the CICE model by Martin et al. (2016) showed that the form drag on ice ridges contributed more than half of C_w for the winter seasons from 1980 to 2010.

C_d is the parameter for determining the form drag force. Bank and Smith (1975) (BS75) obtained a linear form for C_d' as a function of the sail height h' and the

sail slope α'. Garbrecht et al. (1999) continued to summarize a logarithmic approach for the dependence of C_d' on the h' based on measurements of the wind profiles on the leeward side of a pressure ridge. However, these studies were mostly conducted in the atmospheric boundary layer (ABL) over sea ice and only a few cases have been reported for ridge keels in the oceanic boundary layer (OBL). This is mainly because field measurements involving underwater operations in the OBL are difficult, and current meters such as Acoustic Doppler Current Profilers have a blind region in the top 10 cm layer, preventing accurate measurements on layers just under the ice. Therefore, laboratory experiments were performed in a water tank in order to investigate the interaction between ice and water by directly measuring the drag force and altering the test parameters. For example, Pite (1995) found that the keel drag and speed have a quadratic relationship with flow separation and a skin friction relationship without flow separation. However, the depth of the turbulent boundary layer is limited by the fixed flume bottom in the laboratory experiments, this depth is an order of magnitude greater than the depth of the keels in real conditions.

Based on the parameterization scheme of ice-ocean drag coefficient by Lu et al. (2011), we continue to find the parameterization scheme of the form drag coefficient on an individual keel. The motivation of this study was to improve our knowledge of how the form drag on an individual keel varies with keel parameters by combining laboratory experiments and numerical modelling. Moreover, the latter method allowed the experimental results to be extended to the real conditions of the

Arctic Ocean. The manuscript is organized as follows: Section 2 introduces the background of the parameterization scheme on the sea ice drag coefficient. In Section 3, we design the laboratory experimental setup and a numerical model of computational fluid dynamics. The results in terms of the drag force and the drag coefficient of the keel model are presented in Section 4. The numerical model is employed to obtain C_d independent of the water depth, and a discussion of the validity of these results when applied to real conditions takes place in Section 5. Conclusions are drawn in Section 6.

2 Methods

2.1 Parameterization of the ice-ocean drag coefficient

The parametrization of the sea ice drag coefficients, C_a and C_w, is based on the partition concept originating in Arya (1973, 1975) and further developed in the past two decades. The total drag on sea ice is separated into two parts: the skin drag due to the surface shear friction force, and the form drag on floe edges and ice ridges due to the pressure difference across the floes and ridges.

The parametrization of C_a accounts for the effect of sea ice topography parameters, including sea ice concentration, floe size, and ridging intensity, particularly in heavily ridged regions (e.g., coastal and offshore areas) and low ice concentration regions (e.g., marginal ice zone) (Lüpkes et al., 2012). Lu et al. (2011) provided a parameterization scheme of C_w, proposing that the form drag C_R is the dominant factor in large ridging intensity, with C_w expressed as:

$$C_w = C_E + C_R + C_S = f_1 C_e + f_2 C_d + f_3 C_s \quad (1)$$

$$f_1 = \frac{Ad}{2L}\left[1 - \left(\frac{A}{1-A}\,\frac{d}{L}\right)^{1/2}\right]^2 \quad (2)$$

$$f_2 = \frac{Ah}{\pi L_r}\left[1 - \left(\frac{h}{L_r}\right)^{1/2}\right]^2 \quad (3)$$

$$f_3 = A\left(1 - m\frac{h}{L_r}\right) \quad (4)$$

where C_E, C_R, and C_S represent the drag coefficients which contribute, respectively, to form drag by floe edges, form drag on ice ridges, and skin friction on the ice surface. C_e, C_d, and C_s are the local drag coefficients for the contributions of a single floe edge, a single ice ridge, and a uniform ice surface, respectively. f_1 and f_2 represent the shielding effects of upstream floe edges and ice ridges in downstream areas, and they are functions of ice concentration A, floe aspect ratio of draft to length d/L, and the ridging intensity equal to the ratio of keel depth to ridge spacings h/L_r. f_3 is the roughness friction function where m is a constant, equal to 10 in OBL (Lu et al., 2011).

In the above parameterization, C_d is an empirical parameter varying within a wide range. For example, Hoerner (1965) summarized the C_d of waved obstacles on a bottom surface with a smaller slope α with the relationship $C_d = 3.75(\tan\alpha)^2$ (α<20˚). Due to the difference between the bottom surface and the free water surface, C_d was measured at 0.51-0.62 in the flume experiment by Pite et al. (1995). In the calculation of the CICE model by Tsamados et al. (2014), C_d was used as a constant with a range of 0.1-0.3. In Lu's model (Lu et al., 2011), C_d was set as a constant equal to 0.5 according to the measurements under a relatively smooth ice bottom in the Beaufort

164 Sea. The variation of C_d resulted in a proportional variation in the contribution of the
165 ridges in Eq. (1). Different C_d values were related to ridge parameters including the
166 ridge height and the slope angle.

167 2.2 Laboratory experiments

168 C_d is closely related to the Reynolds number *Re*, which reflects the flow
169 pattern (Schlichting, 1960):

170 $$Re = \frac{UL}{\upsilon} \quad (5)$$

171 Here, L is the keel wet length that varies with the keel depth h and the keel slope angle
172 α ($\tan\alpha = 2h/L$), and $\upsilon = 1.003\times10^{-6}\ m^2/s$ is the kinematic viscosity coefficient of water.
173 The flow in the laboratory experiments covered the laminar and turbulent regimes and
174 the transition regime between them. The numerical simulations included only the
175 turbulent flow based on the k-ε turbulence model, corresponding to the real ocean
176 turbulent environment. For different keel shapes, the transition flow regime was
177 related to *Re*. According to a previous dimensional analysis (Zu et al., 2020), C_d can
178 be expressed as $C_d = f(Re, D/h, \alpha)$.

179 The laboratory experiments were performed in a rectangular water tank, which
180 was 0.23 m wide, 4.5 m long, and 0.45 m deep, with glass panels fitted at the sides
181 and the bottom. The ridge keel model was designed to be a wedge-shaped symmetric
182 element using Perspex materials. When the wedge model was driven along the water
183 surface, the drag force of the ridge keel exerted by water was recorded. (Fig. 1).

184 The shape of sea ice ridges in the Arctic Ocean consisted of a triangular sail
185 and a triangular keel in the first-year ridges and a trapezoidal keel in the multi-year
186 ridges (Timco and Burden, 1997; Strub-Klein and Sudom, 2012). The present study
187 focused on the first-year ice using the triangular wedge model for the keel. The slope
188 angle α and the keel depth h were the two control parameters of the keel model. Table
189 1 lists the observed values of these two parameters in real conditions. For the keel
190 slope angle, the normal value was within a range of 20˚–30˚ but the maximum could
191 even reach up to 87.5˚. Therefore, the experimental slope angle was set at 10˚, 20˚,
192 30˚, 45˚, and 90˚. The keel depth varies across a relatively large range and also acted a
193 source of turbulence in the boundary layer under the ice. In this experiment, the ratio
194 D/h was set within a range of 3.5-8.75, where D = 0.35 m is the water depth in the
195 flume.

196 The drift velocity U was also an experimental parameter, and it was set within
197 a range of 0.03-0.3 m/s to reach the turbulent flow conditions as the situation in the
198 turbulent boundary under sea ice. Leppäranta (2011) introduced the notion that the ice
199 drift speed is of the order of 0.01–1 m/s according to a drifting station and acoustic
200 field data.
201

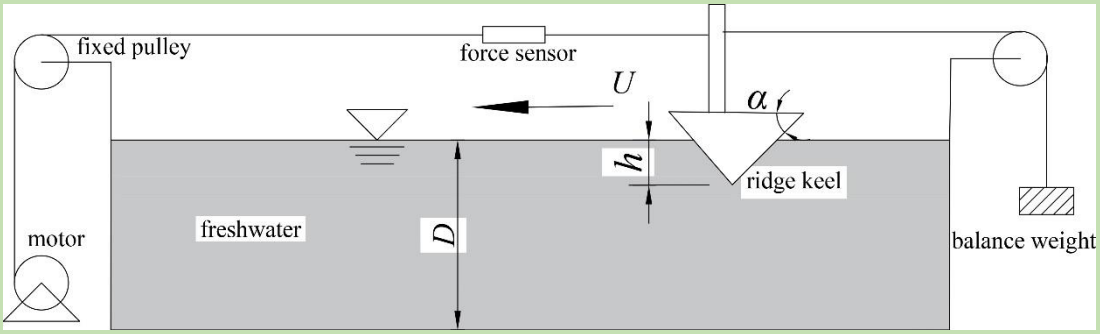

Figure 1. Experimental setup; U is the drift speed of the keel model, h is the keel depth, and α is the keel slope angle.

Table 1. Ridge keel parameters of Arctic first-year ice

Regions	Slope angle/°	Keel depth/m	References
Beaufort Sea and Central Arctic Ocean	26.6 (Mean)	-	Timco and Burden, 1997
East Coast Canada	24.92 (Mean)	2.94 (Mean)	Obert and Brown, 2011
Fram Strait	15–24	5.1–6.7	Sand et al., 2015
Barents Sea	8–29	3.4–7.6	Sand et al., 2015
Shokalsky Strait	11.2–87.5	4.36–4.97	Kharitonov, 2020

2.3 Numerical Simulation

Numerical experiments were conducted as for an additional view and to further extend the results of the laboratory experiments. In particular, the flume study was limited by the fixed, finite water depth. Provided the hydrodynamic similarity is satisfied, the flow in the numerical flume past the ridge keel at a uniform upstream velocity and the drag force of the ridge keel should be the same as the results in the flume experiments, where the keel moves at the same speed in the stationary fluid.

Considering the symmetry of the flow field and the slight variations along the transverse section of ridge model, the numerical simulation was simplified to be a two-dimensional flow problem; namely, the vertical cross section along the length of the flume is chosen as the computational domain (Fig. 2). To ensure a fully developed wake flow on the lee side of the ice floe, the ridge model was placed a third of the way down the flume, agreeing with the general conditions for a fully developed wake flow. The control equations for the flow field used the *k*-ε turbulence model (Launder and Spalding, 1972). The momentum equation is written as:

$$\frac{\partial u_i}{\partial t} + u_j \frac{\partial u_i}{\partial x_j} = -\frac{1}{\rho}\frac{\partial p}{\partial x_i} + \frac{1}{\rho}\frac{\partial}{\partial x_j}\left(\mu\left(\frac{\partial u_i}{\partial x_j} + \frac{\partial u_j}{\partial x_i}\right) + \tau_{ij}\right) \quad (6)$$

where u_i denotes the velocity components in the Cartesian coordinates x_i, t is time, ρ is water density, p is pressure, μ is the dynamic water viscosity coefficient, and τ_{ij} is the Reynold stress, which is related to the mean velocity gradients as per the Boussinesq hypothesis of an isotropic eddy viscosity μ_t (Hinze, 1975):

$$\tau_{ij} = \mu_t\left(\frac{\partial u_i}{\partial x_j} + \frac{\partial u_j}{\partial x_i}\right) - \frac{2}{3}k\delta_{ij} \quad (7)$$

where k is the turbulent kinetic energy and δ_{ij} is the Kronecker delta. The fluid flow was solved with the RANS code supplied by the commercial software, FLUENT. It was based on the finite volume method, and the discretization schemes adopted the second-order upwind method in space and were steady in time. Equations were solved using the SIMPLEC algorithm. For the RNG *k*-ε two equation model, C_μ=0.0845, $C_{1\varepsilon}$=1.42, $C_{2\varepsilon}$=1.68, and α_ε=α_k=1.39 (Yakhot and Orszag, 1986; Orszag et al., 1993). Along the boundary of the keel, Reynolds stresses were zero due to the presence of a

236 viscous sublayer and affect the distribution of the pressure p in the keel boundary.
237 Normal stresses originated from the pressure p that was exerted on the keel. Therefore,
238 the total keel drag could be obtained by integrating the frictional stresses and normal
239 stresses along the keel boundary.

240 $$F = \int_{x=-h\tan\alpha}^{x=h\tan\alpha} [\mu \left(\frac{\partial u}{\partial z} + \frac{\partial w}{\partial x}\right) n_z + \left(p + 2\mu \frac{\partial u}{\partial x}\right) n_x]_{z=\eta(x)} dx \quad (8)$$

241 Keel shape function is defined as $z=\eta(x)$, $-h\tan\alpha<x<h\tan\alpha$.

242 $$\eta(x)=\tan\alpha x+D-h,\ 0\leqslant x\leqslant h\tan\alpha;$$

243 $$-\tan\alpha x+D-h,\ -h\tan\alpha\leqslant x<0.$$

244 The fluctuation of the free surface is regarded as very small, so it is ignored.
245 Furthermore, a rigid lid assumption is employed for the free surface AB and DE
246 (shown in Fig. 2), when $z=D$:

247 $$w=0,\ p=p_a.$$

248 where p_a is the atmosphere pressure, which here is set as zero. At the bottom and at
249 the keel boundary (when $z=\eta(x)$ and $z=0$), there are no-slip boundary conditions:

250 $$u=w=0.$$

251 The boundary conditions at the velocity inlet and outlet are given by,
252 respectively:

253 $$u=U \text{ and } w=0,$$
$$\frac{\partial u}{\partial x} = \frac{\partial w}{\partial x} = 0$$

254 The outlet boundary is far from the disturbance region, so the gradient of
255 velocity in the x direction is zero. We chose typical cases with a slope angle of 45° for
256 computation to test the independence of the grid size. When the space size was set to

257 between 0.5 cm and 0.9 cm, the calculation was stable. We chose 0.5 cm as the final
258 grid size.
259

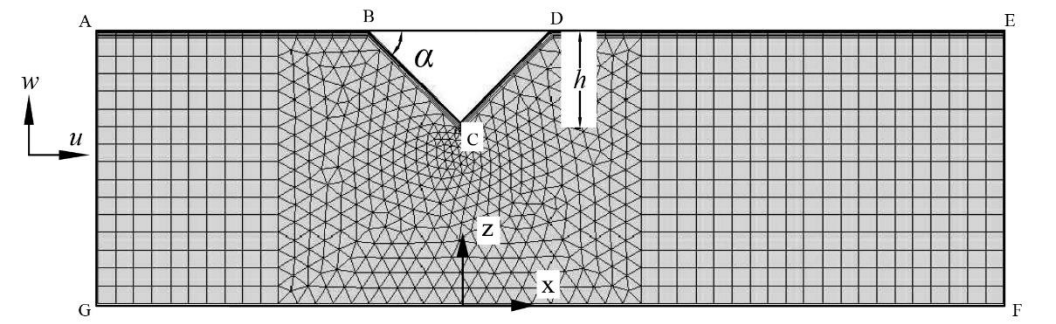

260

261 **Figure 2.** Numerical computational domain. *u* and *w* are fluid velocities respectively
262 in the *x* and *z* direction, α is the keel slope angle, and *h* is the keel depth into the water.
263 Near the keel there are unstructured grid cells.
264

265 **3 Results and Discussion**

266 3.1 Local form drag coefficient

267 The drag force was measured using a tension sensor in the laboratory
268 experiments. We used the drag force *F* on a unit length of a two-dimensional keel
269 model to obtain C_d. In the numerical simulation, this drag force was calculated by Eq.
270 (8). *F* and C_d have a quadratic relationship:

271 $$F = 0.5 C_d \rho h U^2 \quad (9)$$

272 where *U* is the drift velocity of the ridge, and the water density is taken as ρ = 998.2
273 kg/m^3. The dependency of C_d on the Reynolds number is shown in Fig. 3. It is clear
274 from Fig. 3 that C_d decreased linearly with an increasing *Re* in the laminar region up
275 to Re $\approx 1\times10^4$. As *Re* > 1×10^5, the flow in the experimental flume was fully

276 turbulent, with C_d independent of *Re*. At *Re* ~ 10^4-10^5, the laminar-turbulent transition
277 regime was found, with C_d(*Re*) adapting between the linear decrease and the fixed
278 level. Turbulence started at a lower Re for sharper keels because the disturbance of
279 flow was stronger near to sharper keels.
280

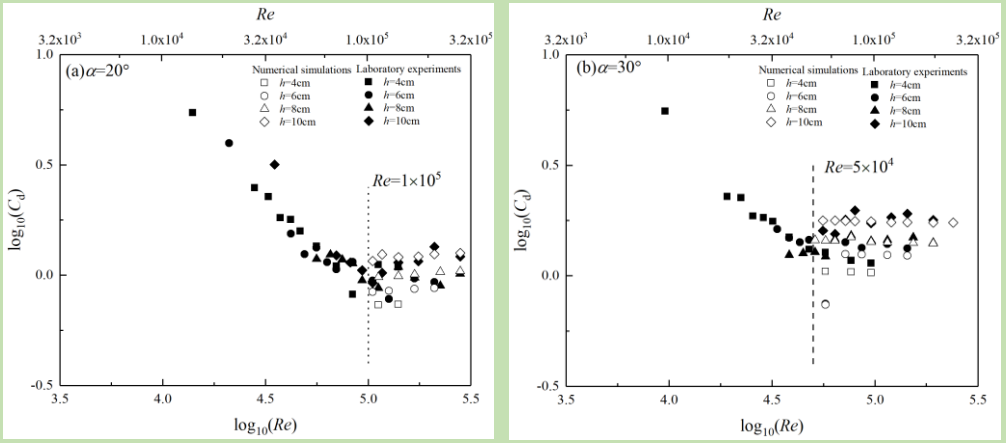

281

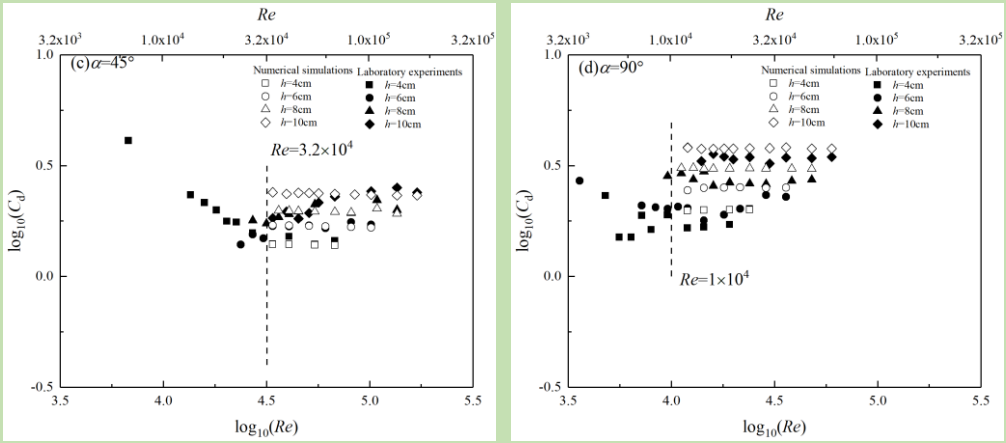

282

283 **Figure 3.** Plots of $\log_{10}(C_d)$ with $\log_{10}(Re)$ at keel depths *h*=4cm (■, □), 6cm (●, ○),
284 8cm (▲, △), and 10cm (◇, ◆). Empty dots represent numerical results and solid
285 dots represent laboratory results. The keel slope angle α is (**a**) 20˚, (**b**) 30˚, (**c**) 45˚,
286 and (**d**) 90˚. The part to the right of the vertical dashed lines the is absolutely turbulent
287 flow. The critical Reynolds numbers are, respectively, (**a**) 1×10^5 for α=20˚, (**b**) 5×10^4

288 for α=30˚, (**c**) 3.2×10^4 for α=45˚, and (**d**) 1×10^4 for α=90˚.

289

290 For the fully turbulent regime, the numerical results mostly agreed well with
291 laboratory experiments. At large slope angles, the fit became worse. At α = 90˚, the
292 numerical results were a little larger than the laboratory outcome because a flow
293 separation existed at the sharp wedge. Fig. 3 shows that C_d varied within 0.17–3.78
294 with h and α. The maximum value of the ratio D/h was 8.75 in this experiment due to
295 the limitation of the flume depth. Thus, the flow past the keel model was narrow and
296 it had an impact on the variation of the resulting drag coefficient with a keel depth h.

297 3.2 Difference between laminar and turbulent flow

298 The experimental results in the laminar flow regime are summarized in Fig. 4.
299 The friction coefficient of a flat plate was proportional to $Re^{-0.5}$ (Hoerner, 1965).
300 Using the linear least squares regression, this study obtained the relation $\log_{10}(C_d)$
301 $=-0.5\log_{10}(Re)+2.5$. The correlation coefficient was R = 0.87. The linear regression
302 passed the significance test (F-test, $p<<1\times10^{-3}$). In the laminar region, viscous shear
303 stress dominated the drag force and C_d only depended on Re.

304

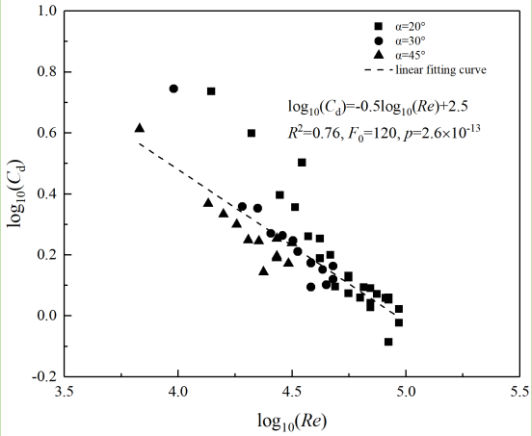

Figure 4. Plots of laminar flow results for all keel shapes and linear least squares regression fit.

C_d was no longer associated with *Re* in turbulent flow. Then, the streamlines around the keel model were no longer smooth, and a vortex wake was formed at the lee side. The pressure in the vortex zone was lower than the pressure at the same horizontal level at the front, and the form drag force created by the pressure difference was much greater than the skin friction drag force. The variation of C_d with D/h when U = 0.15 m/s and $\alpha = 45^{\circ}$ is shown in Fig. 5a as an example. In other cases with the constant U and α, the variations of C_d with D/h were all similar in a turbulent flow.

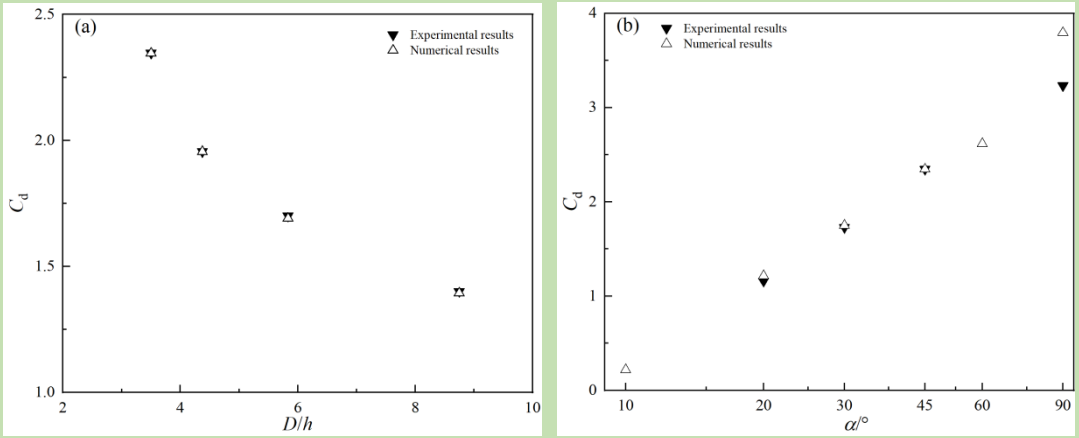

317 **Figure 5.** The variation of C_d with (**a**) D/h (h=4 cm, 6 cm, 8 cm, and 10 cm, D=35
318 cm) when U=0.15 m/s and α=45˚ and (**b**) α (10˚≤α≤90˚) when U=0.15 m/s and h =10
319 cm in experimental and numerical results (note: log scale for α).
320
321 It is clear from Fig. 5a that C_d decreased with D/h. The total drag force was
322 determined by the size and shape of the keel model, which decided the distribution of
323 pressure around the keel. Physical experiments were conducted in the tank with a
324 finite depth. For the flow past the keel, there was a sheltered area behind the keel
325 (Garbrecht et al., 1999). With the increase in h, the flow passage channel became
326 narrower. The upstream-downstream pressure difference $\triangle p$ was proportional to
327 $0.5\rho\triangle U^2$ according to the Bernoulli equation in fluid dynamics. According to the law
328 of mass conservation, it can be seen that $0.5\triangle U^2 = 0.5(h/(D-h))^2U^2$. Consequently, C_d
329 $\sim \triangle p/\rho U^2 = 0.5/(D/h-1)^2$. Based on the inviscid flow theory, the increase in C_d with
330 D/h was nonlinear, especially when $2 < D/h < 10$ (Fig. 5a). As D increased, the
331 influence of h on C_d weakened with $C_d \rightarrow 1.2$ for $D >> h$. In real conditions, the depth
332 of the mixed layer was an order of magnitude greater than the keel depth. Thus, the
333 keel movement in a deeper tank would be more appropriate, but by scaling the
334 analysis our results were suitably applicable to nature-scale conditions.

335 For U=0.15 m/s and h=10 cm, $Re > 10^5$, and the flow was fully turbulent for all
336 keel shapes. Fig. 5b shows that C_d increases linearly with ln(α). The slope angle α was
337 a key parameter of the keel shape for the influence on C_d. It was obvious (Figs. 3 and

338 5) that the numerical results agreed well with the physical experiments in the turbulent
339 regime. Therefore, we could use this turbulent model to examine cases of keels in
340 deeper water.
341
342 3.3 Applications to real conditions
343 In the Arctic Ocean, turbulence in OBL is generated by winds, surfaces heat
344 fluxes, and the drift of sea ice. The mixed layer depth in OBL is often determined by
345 the vertical temperature and density distribution, and it is about 50 m in idealized
346 ocean-ice models (Steele and Boyd, 1998; Beer et al., 2020). McPhee (2002)
347 measured the mixed layer depth of 25 m in the boundary layer under ice using a CTD
348 sounding device during the SHEBA drift. Strub-Klein and Sudom (2012) analyzed
349 186 ridge keels in an Arctic region and obtained an average keel depth of 4.8 m, but
350 keel depths vary from zero up to more than the OBL depth. Thus, the ratio of the
351 turbulent OBL depth to the mean keel depth in the Arctic seas is around 10, but the
352 range of variation is large.

353 Our study focused on the drag force in homogeneous fluids, which resembled
354 the mixed layer in real conditions because the bottom thin boundary layer had little
355 effect on the uniform velocity field in the flume. Fig. 6a shows the different variation
356 law of C_d with h and D. When D/h >10, C_d tended to be stable, as shown in Fig. 6b.
357 When D/h <10, the keel depth induced disturbances around the halocline, and internal
358 waves were also generated in an ice-covered ocean (Fer et al., 2014; McPhee, 2002;

359 Pite et al., 1995), which will be considered in further studies. Thus, D/h>10 was set as
360 a criterion which decides that the C_d results in this study can be applied to real
361 conditions.

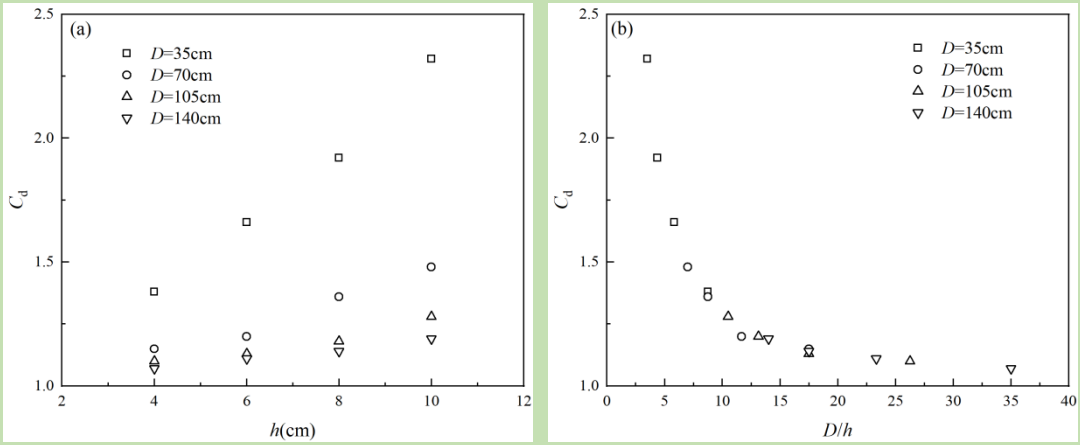

362

363 **Figure 6.** (**a**) Variation of C_d with h and D for U=0.3 m/s (turbulent regime) and
364 α=45˚, and (**b**) the dimensionless relationship between C_d and D/h.

365

366 To extend the results in Fig. 3 to real conditions, we used the numerical k-ε
367 turbulence model. First, the sensitivity of the results from the model to the water
368 depth was investigated, and the simulated drag coefficient is shown in Fig. 7. C_d
369 decreased rapidly to about half the original value, when the water depth D increased
370 to three times the original D=35 cm. However, when D continued to increase and
371 reached D=140 cm (four times the original), C_d tended to be stable, and the difference
372 from the case of D=105 cm was less than 4%. Therefore, we used D=140 cm as an
373 independent water depth where the bottom boundary only had a minor effect on flow
374 past the keel.

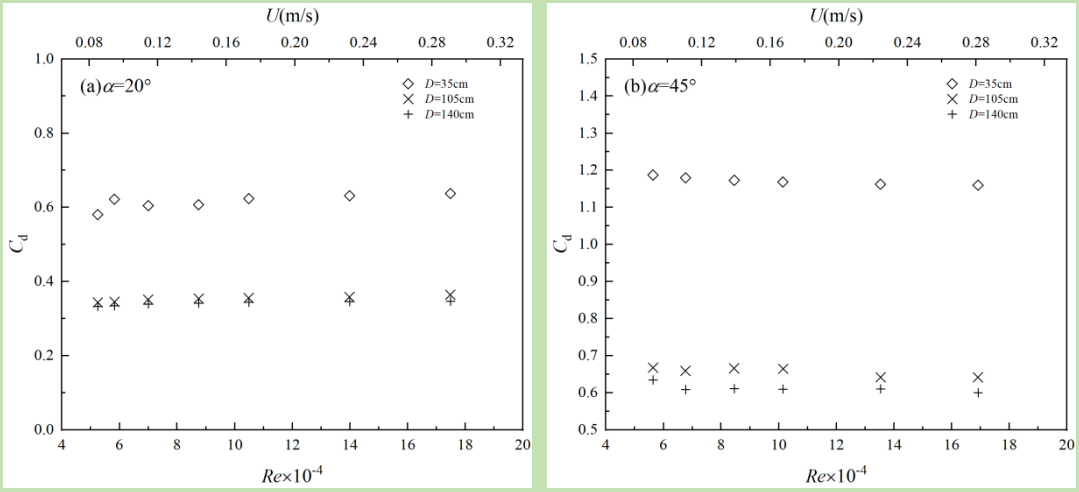

Figure 7. C_d vs. *Re* in the numerical simulations at different water depths, *D*=35 cm, 105 cm, and 140 cm, when *h*=10 cm, (**a**) $\alpha = 20^{\circ}$ and (**b**) $\alpha = 45^{\circ}$.

The length of the calculation field had no effect on the results because the fluid outlet had been restored to a uniform flow. Thus, the results of C_d in a turbulent flow could be extended to an independent water depth, as shown in Fig. 8.

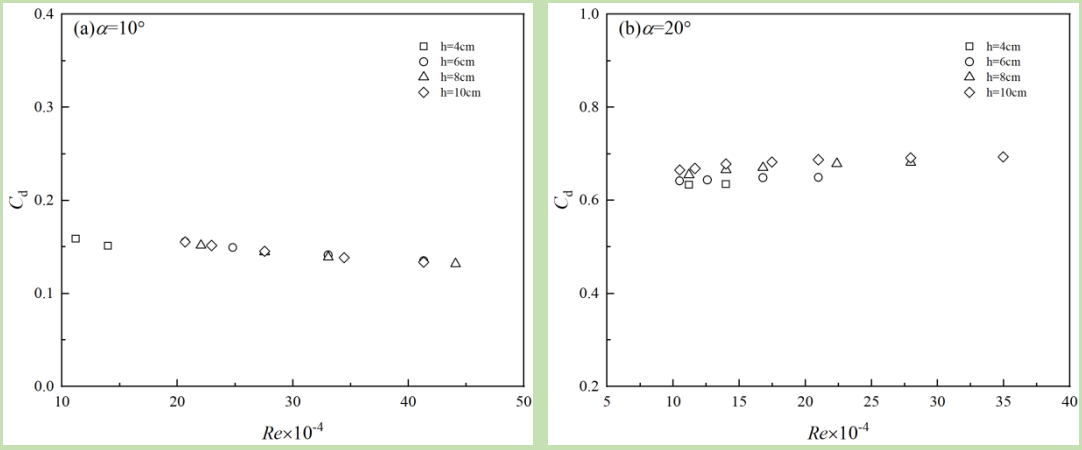

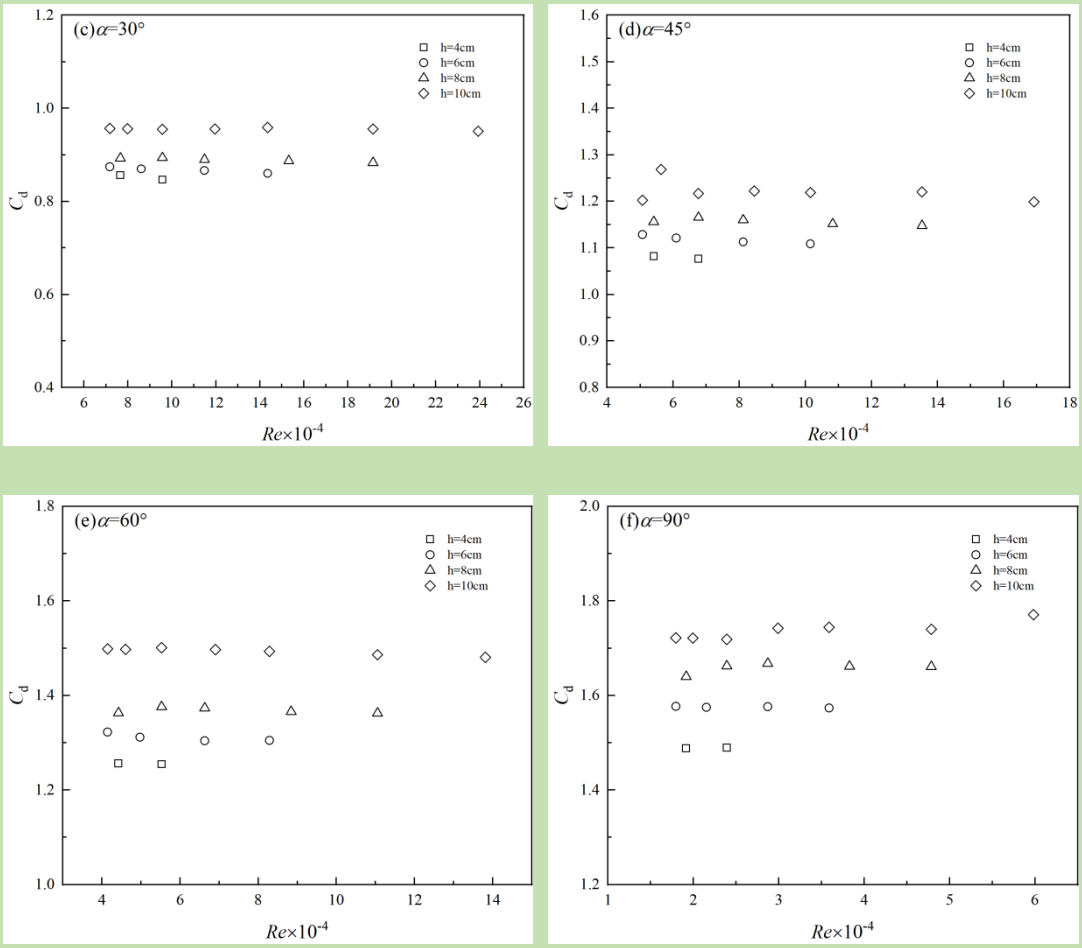

Figure 8. Independent C_d results on water depth obtained from a numerical turbulence model when h=4 cm, 6 cm, 8 cm, and 10 cm, (**a**) α = 10˚, (**b**) α = 20˚, (**c**) α = 30˚, (**d**) α = 45˚, (**e**) α = 60˚, and (**f**) α = 90˚.

C_d tended to be stable with *Re* at a constant keel angle in the turbulent regime. However, the variation of C_d with h was much smaller than the results in Fig. 5 with a shallow depth, where we obtained C_d~$0.5/(D/h\text{-}1)^2$ based on the inviscid theory. When D=140 cm, D/h>14, and the variation of h only has a minor effect on C_d. For example, C_d increased less than 1% from h=4 cm to h=10 cm when α = 20˚. For the larger α, h still had some influence on C_d, as shown in Fig. 8, because the shelter area

behind a sharp keel increased more with h than compared with a flat keel. However, this influence was much smaller than at D=35 cm (Fig. 5a); the keel angle α had a significant influence on C_d, which was similar to the variation laws shown in Fig. 5b.

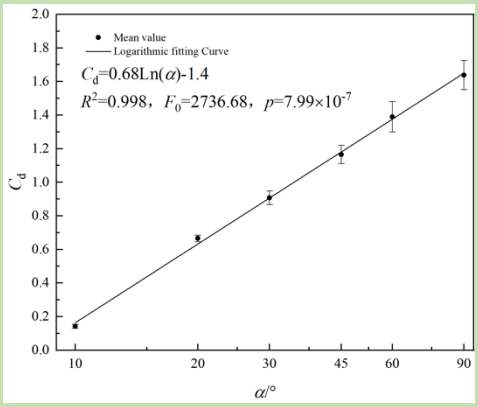

Figure 9. Relationship between C_d and α for real ocean conditions.

Fig. 9 illustrates that C_d increases from 0.17 to 1.66 in the keel angle range of 10˚-90˚. A logarithmic fit was determined as:

$$C_d=0.68\ln(\alpha/7.8°),\ 10° < \alpha < 90° \quad (10)$$

The squared correlation coefficient was R^2=0.998, which was comfortably past the significance level (F test, F_0 =2736.68>$F_{0.005}$(1, 4) =31.3 and p{F>F_0} ~ 10^{-6}).

The variation of C_d in Fig.9 with keel slopes included all laboratory cases. However, field observations and underwater sonar data showed that keel slopes had a log-normal distribution and more than 80% of keel slopes were concentrated within a range 10˚–50˚; the mean value was 23.2˚ in Davis and Wadhmas (1995) and 26.6˚ in Timco and Burden (1997). The range of C_d in Arctic conditions was 0.17–1.26, corresponding to the slope angle range 10˚-50˚; for a representative slope angle 25°, C_d = 0.79. This range was larger than the range in the form drag of ridge sails, C_d'

(the apostrophe representing air-ice parameters hereinafter), which has been summarized as 0.2-0.8 (Garbrecht et al., 1999). Banke et al. (1976) summarized the field observation data on the air-ice interface and obtained a linear relationship between C_d' and α': $C_d'=0.012+0.012\alpha'$. Tsamados et al. (2014) used a C_d range of 0.1-0.3 for both ABL and OBL in the CICE sea ice model. However, our results show that C_d is larger than C_d', and that it is unreasonable to take C_d as a constant, which was done in previous sea ice models.

The result of C_d in Eq. (10) ignored the effect of h and adopts the mean value keel depth in the Arctic. It was valid as long as $D/h>10$. Although h was an important morphology parameter of keels, it was only for large keels that the depth had a notable influence on the form drag, which will induce internal waves around pycnocline. In sea ice dynamics modelling, the form drag forces exerted along the keels were converted to the horizontal stress per unit area. For multiple keels, the drag coefficient on keels C_R varied with the ratio of keel depth to keel spacing h/L_r because h represented the statistical distribution of keel depths; with a larger h, there were more deep keels. We only considered the effect of α in the parametrization of C_d for an individual keel with $h<<D$, but for multiple keels, h was still an important parameter, as shown in Eq. (3).

3.4 Dominance of ridge form drag

Considering the combined impact of multiple floes and ice ridges in Eqs. (1)-(4), the total ice-ocean drag coefficient, C_w, and the contribution of form drag on

436 ridge keels, C_R, could be determined in a simple manner. In the calculations, d/L, the
437 ratio of ice draft to floe length, was set as 0.01 for simplicity by Lu et al. (2011),
438 where floe edge drag was the main part of the total drag for a moderate ice
439 concentration. However, the keel drag component may change the dominance over the
440 floe edge drag proportion. The order of h/L_r varied from 10^{-3} to 10^{-1} according to
441 investigations by Davis and Wadhams (1995), who analyzed a sonar data set
442 comprising 729 ridges on a submarine cruise between Greenland and Svalbard from
443 78˚N to 90˚N. Other parameters of this drag force analysis are listed in Table 2, the
444 selection basis will be explained in the next section, and the results are shown in Fig.
445 10.

446 Fig. 10a shows the variation of C_R with α and h/L_r when A=60%, representing
447 moderate ice concentrations. Due to the influence of α on C_d, C_R varied greatly. C_R
448 increased quickly with the increase in α for $10^{\circ}\leq\alpha\leq50^{\circ}$and $h/L_r \geq10^{-2}$, from 0.01×10^{-3}
449 to 11.29×10^{-3}. A similar trend of C_R with α and A is shown in Fig. 10b, where h/L_r =
450 0.05, adopting the mean spacing of statistical data of keels deeper than 5 m for 2004
451 and 2007 from North Greenland by Wadhams et al. (2011). C_R was sensitive to α at a
452 larger A, and increased especially quickly in the α range of 10˚-50˚, from 1.62×10^{-3} to
453 12.13×10^{-3} with A=100%.

454 Fig. 10c shows the variation of C_R/C_w with α and h/L_r when A=60%. C_R/C_w
455 was more than 50% as $h/L_r\geq$ 0.05. The contribution of C_R increased rapidly with the
456 variation of α for $20^{\circ}\leq\alpha\leq50^{\circ}$when h/L_r=0.05, from 56.6% to 71.6%. It is shown in Fig.

457 10d that the variation of C_R/C_w was very dramatic at α<20˚ due to the gradient of C_R

458 to α being relatively large with the logarithmic relationship, and C_R increased quickly.

459 There was a similar variation law of C_R/C_w at A>90% because C_E even decreased

460 with an increase in A at high ice concentrations. In other cases, the variation of C_R/C_w

461 with α and A was relatively small.

462

463

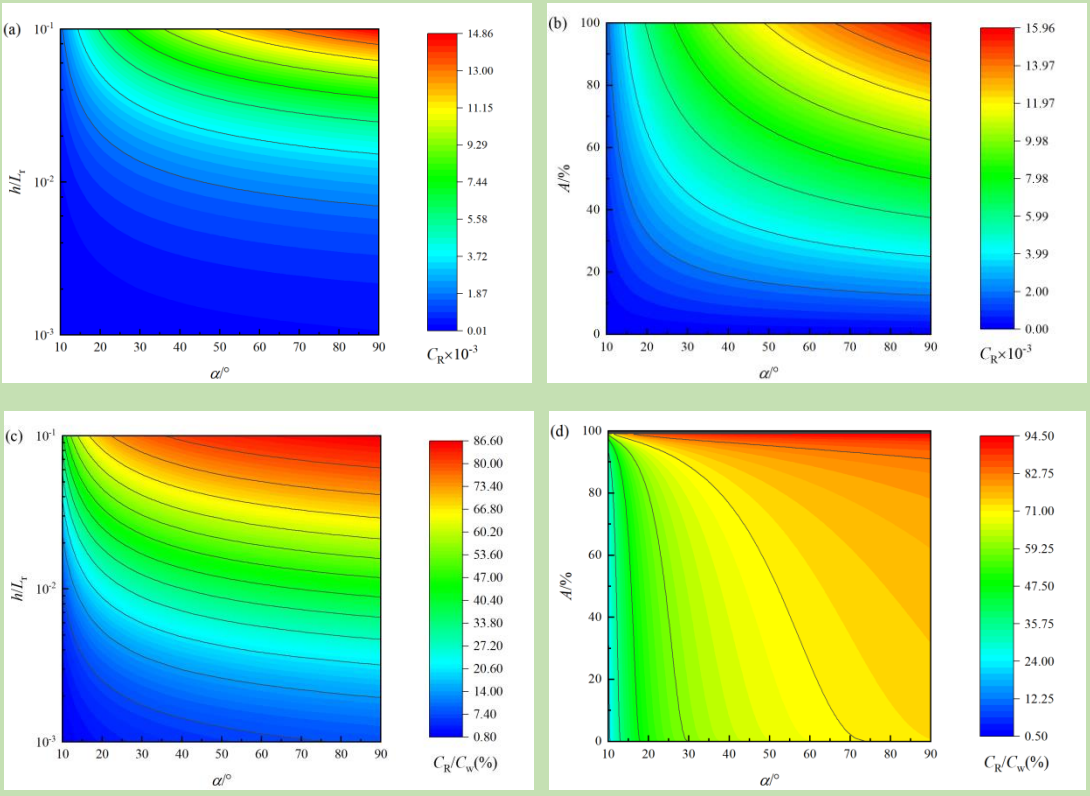

464

465 **Figure 10.** Variations of C_R with (**a**) α and h/L_r when A=60% and (**b**) α and A when

466 h/L_r=0.05 and variations of C_R/C_w with (**c**) α and h/L_r when A=60% and (**d**) α and A

467 when h/L_r=0.05.

468

3.5 On C_a/C_w

The relationship between the air-ice drag coefficient C_a and the ice-ocean drag coefficient C_w was interesting in sea ice dynamics research and modelling. In steady wind-driven free ice drift, the drift speed is proportional to $(C_a/C_w)^{1/2}$ (Leppäranta, 2011). Because the field observations of air-ice interaction are relatively easy to perform compared with underwater experiments, there is abundant literature on C_a (Banke et al., 1976; Overland, 1985; Anderson, 1987; Leppäranta and Omstedt, 1990; Gabrecht et al., 1999; Lüpkes et al., 2012). Combined with the results of this study, it was easy to investigate the variations of C_a/C_w at different sea ice conditions if the correlations between the ice surface and the bottom topography are pre-defined.

The formation of ice ridges mainly arises due to the mutual squeezing of sea ice, and the morphology characteristics of upper and lower surfaces are therefore related to some degree (Leppäranta, 2011). Relevant parameters on the sea ice surface and the bottom are listed in Table 2. For ridge slopes, sail angles vary at a similar range to keels, and the average angle is 19.2˚ (Strub-Klein and Sudom, 2012). Timco and Burden (1997) found that both keel angles and sail angles have a lognormal distribution at a wide range, from 10˚ to 80˚ in Arctic seas, and the mean value of the sail angles is 20.7˚, which is slightly smaller than the 26.6˚ of the keel angles. In order to facilitate the calculation of the effect of α on C_a/C_w, keel angles and sail angles are assumed to be the same in the following discussion. The keel-to-sail ratio h/h' has been fitted to a log-normal distribution for first-year ridges (Timco and Burden,

1997). Kharitonov et al. (2020) found recently that h/h' is about 3. For freeboard d' and draft d of level ice, the ratio d/d' is different from the ratio h/h' of ridges. Wadhams and Doble (2008) investigated in situ measurements of snow and level ice in a 100×110 m area by drilling holes in the spring Beaufort Sea, and found that median ice draft (d) was 137 ± 15 (standard deviation) cm, with an ice freeboard (d') of 13 ± 5 cm. According to the Archimedes principle and the standard isostatic relation, $d/d'=\rho_i/(\rho_w-\rho_i)$, where ρ_i is ice density and ρ_w is seawater density when the snow cover is ignored. We selected ρ_i=918 kg/m^3 and ρ_w=1021 kg/m^3 (Dobel et al., 2011), and d/d'=8.9 was the result. In the calculation of C_a/C_w, d'/d was selected as 1/10, and A varied across a range of 0-100% in time and space.

Table 2. Morphology of sea ice surface and bottom

Ice parameters	Bottom	Surface
Keel or sail slope angle	α=10˚-90˚	$\alpha'=\alpha$
Ratio of keel depth or sail height to ridges interval distance	h/L_r=0.001-0.1	$h'/L_r=1/3h/L_r$
Ratio of ice draft or freeboard to floe length	d/L=0.01	$d'/L=1/10d/L$
Ice concentration	A=0-100%	A=0-100%
Local ice lateral coefficient	C_e=1	C_e'=1
Local form coefficient on a keel or sail	C_d=0.68ln(α/7.8)	C_d'=0.012+0.012α'
Local ice frictional coefficient	C_s=0.002	C_s'=0.002

The variation of C_a/C_w is shown in Fig. 11. This ratio ranged from 20.9% to 41.8% with α and h/L_r for moderate ice concentrations (A=60% Fig. 11a). This meant

505 that the free drift speed of ridged ice was lower by up to about 1/3 compared with
506 ridged ice. When h/L_r was relatively low (h/L_r <0.01), C_a/C_w decreased monotonically
507 with the increase in α, and the effect of α on C_a/C_w is weak. Because ridge slopes only
508 contributed to their form drag, the floe edge form drag and skin friction drag are the
509 dominant parts with a low h/L_r. Then, C_a/C_w was relatively high and is influenced by
510 other parameters such as the hydrodynamic roughness of the ice surface. When h/L_r
511 was relatively high (h/L_r > 0.01), C_a/C_w first decreased and then increased with the
512 increase in α. At this time, C_d played a key role in C_a and C_w, and the difference of C_d
513 between keels and sails reached a maximum at about α=30˚. Also, the momentum
514 exchange between the air and the water reaches the maximum. Fig. 11b also shows
515 that C_a/C_w reached a minimum at about α=30˚ with h/L_r=0.05. In this case, the
516 component of frictional coefficient C_S' in C_a was more important than C_S in C_w.
517 Compared with C_R', C_S' increased more quickly. Despite C_R dominating C_w, C_a/C_w
518 increased with the increase in A in Fig. 11b.
519

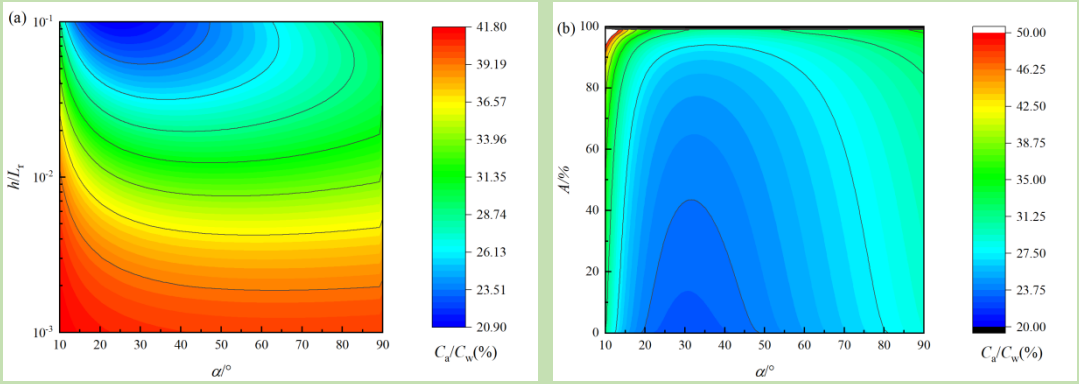

520

521 **Figure 11.** Variation of C_a/C_w with (**a**) α and h/L_r when A=60% and (**b**) α and A when
522 h/L_r=0.05.

4 Conclusion

Laboratory experiments and numerical simulations were conducted to study the keel motion and drag force in homogeneous fluids. The momentum flux from a fluid to a keel model was provided through the form drag coefficient C_d. Regarding the laminar flow regime, the friction drag force was the main part of the total force, and the shape of a keel had little effect on C_d. With the turbulent regime, the results of the numerical simulation agreed well with laboratory data. C_d was sensitive to the shape of a keel described by h and α and tends to a stable level with a very large Re. It was shown that when $h << D$, the depth of the water layer, the local form drag coefficient was independent of h but sensitive to the keel slope angle α.

In order to eliminate the effect of the bottom boundary of the flume, we used numerical simulations to obtain a C_d independent of the water depth. This independent C_d was not sensitive to keel depth, but was closely related to the keel slope angle. We used a logarithmic function and obtained the relationship $C_d=0.68\ln(\alpha/7.8)$, $10^\circ\leq\alpha\leq90^\circ$, varying from 0.14 to 1.64. Based on the parameterization concept, $C_d=0.68\ln(\alpha/7.8)$ could be applied to sea ice modelling. For moderate ridging intensity and ice concentrations, C_R increased monotonically and quickly in the α range of 10˚–50˚ and becomes the dominant part of C_w when $\alpha\geq20^\circ$. Pressure ridges in the Arctic region have a large variability in morphology characteristics, and the keel slope angles are mainly distributed from 10˚ to 50˚ (Davis and Wadhmas, 1995;

544 Timco and Burden, 1997; Obert and Brown, 2011; Strub-Klein and Sudom, 2012). It
545 was obvious that the variation of α had a significant influence on C_R and C_R/C_w and
546 should be taken into account in sea ice dynamic models.

547 C_a/C_w varied from 20.9%-41.8% with α and h/L_r for moderate ice
548 concentrations (A=60%) and had a relative low value variability at A and α=30˚. The
549 wind factor represents the ratio of ice velocity to wind velocity for wind-driven sea
550 ice drift. In the free drift case, the wind factor tended to the Nansen number *Na*,
551 $Na=0.036\sqrt{(C_a/C_w)}$. *Na* is about 1.6%–2.3%, corresponding to the C_a/C_w range of
552 20.9%-41.8% in Fig. 11. It agreed with the value collected by field observations in the
553 Arctic Ocean (Leppäranta, 2011). Thus, in this simple case, the velocity of sea ice was
554 proportional to *Na*, which increased with the decrease in α where α<30˚. With the
555 rapid decay of Arctic sea ice in recent years, the morphology parameters of sea ice
556 have also been changing, and the temporal and spatial characteristics vary. In
557 multi-category sea ice models, the ice thickness distribution could be adjusted with a
558 dynamic and a thermodynamic process. Thinner sea ice may be more easily subjected
559 to deformation, resulting in sea ice ridging or hummock ice (Lepparänta, 2011). The
560 redistribution of deformed and undeformed ice also had an influence on the
561 morphology of ice; thus, the slope angle of ridged ice as well as the amount of ridging
562 further affected the drift of sea ice. The decreasing trend of *Na*, where α<30˚, caused
563 an increase in the free drift speed of sea ice.

Therefore, ridge keel morphology needed to be taken account in the parameterization of C_d, which laid the foundation for the parameterization of the ice-water drag coefficient in mesoscale and large-scale sea ice models. In heavily ridged regions, the accurate local drag coefficient was crucial in sea ice forecasting in the short-term, as well as in climatological models. In addition to the influence of keel shapes, two questions require further research. First, for large keels, when the keel depth approaches the depth of the mixed layer, the keel depth became important in addition to the shape. Secondly, the flow stratification also had an effect on C_d. Thus, further experimental research and theoretical analysis are required to establish an advanced parameterization scheme for the sea ice–ocean drag coefficient.

Acknowledgements

This research was supported by the National Key R&D Program of China No 2018YFA0605900, the National Natural Science Foundation of China (Grant No. 41922045 and 41876213), the Academy of Finland (Grant No. 333889 and 317999), and the Fundamental Research Funds for the Central Universities (DUT20GJ206).

Data Availability Statement

The experimental and numerical dataset in this research can be accessed via the website (https://doi.org/10.5281/zenodo.4270715).

References

Anderson, R. J. (1987). Wind stress measurements over rough ice during the 1984 Marginal Ice Zone Experiment. *Journal of Geophysical Research, 92*(C7), 6933-6941.

585 https://doi.org/10.1029/JC092iC07p06933

586 Arya, S. P. S. (1973). Contribution of form drag on pressure ridges to the air stress on
587 arctic ice. *Journal of Geophysical Research*, *78*(30), 7092-7099.
588 https://doi.org/10.1029/JC078i030p07092

589 Arya, S. P. S. (1975). A drag partition theory for determining the large-scale roughness
590 parameter and wind stress on the Arctic pack ice. *Journal of Geophysical Research*,
591 *80*(24), 3447-3454. https://doi.org/10.1029/JC080i024p03447

592 Banke, E. G., & Smith S. D. (1975). Measurement of form drag on ice ridges. *AIDJEX*
593 *Bull*., 28, 21–27.

594 Banke, E. G., Smith, S. D., & Anderson, R. J. (1976). Recent measurements of wind
595 stress on Arctic sea ice. *Journal of the Fisheries Research Board of Canada*, *33*(10),
596 2307-2317. https://doi.org/10.1139/f76-277

597 Banke, E. G., Smith, S. D., & Anderson, R. J. (1980). Drag coefficients at AIDJEX
598 from sonic anemometer measurements. *Sea Ice Processes and Models*, 430-442.

599 Beer, E., Eisenman, I., & Wagner, T. J. W. (2020). Polar amplification due to enhanced
600 heat flux across the halocline. *Geophysical Research Letters*, *47*(4).
601 https://doi.org/10.1029/2019GL086706

602 Blackadar, A. K., & Tennekes, H. (1968) Asymptotic similarity in neutral barotropic
603 planetary boundary layers. *Journal of the Atmospheric Sciences*, *25*(6), 1015-1020.
604 https://doi.org/10.1175/1520-0469(1968)025<1015:ASINBP>2.0.CO;2

605 Castellani, G., Lüpkes, C., Hendricks, S., & Gerdes, R. (2014). Variability of Arctic
606 sea-ice topography and its impact on the atmospheric surface drag. *Journal of*
607 *Geophysical Research: Oceans*, *119*(10), 6743-6762.
608 https://doi.org/10.1002/2013JC009712

609 Comiso, J. C. (2012). Large decadal decline of the Arctic multiyear ice cover. *Journal*
610 *of Climate*, *25*(4), 1176-1193. https://doi.org/10.1175/JCLI-D-11-00113.1

611 Davis, N. R., & Wadhams, P. (1995). A statistical analysis of Arctic pressure ridge
612 morphology. *Journal of Geophysical Research*, *100*(C6), 10915-10925.
613 https://doi.org/10.1029/95JC00007

614 Doble, M. J., Skourup, H., Wadhams, P. & Geiger, C. A. (2011). The relation between
615 arctic sea ice surface elevation and draft: a case study using coincident AUV sonar
616 and airborne scanning laser. *Journal of Geophysical Research*, *116*, C00E03.
617 https://doi:10.1029/2011JC00707

618 Fer, I. (2014). Near-Inertial Mixing in the Central Arctic Ocean. *Journal of Physical*
619 *Oceanography*, *44*(8), 2031-2049. https://doi.org/10.1175/JPO-D-13-0133.1

620 Garbrecht, T., Lüpkes, C., Augstein, E., & Wamser, C. (1999). Influence of a sea ice
621 ridge on low-level airflow. *Journal of Geophysical Research*, *104*(D20), 24499-24507.
622 https://doi.org/10.1029/1999JD90048

623 Garbrecht, T., Lüpkes, C., Hartmann, J., & Wolff, M. (2002). Atmospheric drag
624 coefficients over sea ice–validation of a parameterisation concept. *Tellus A: Dynamic*

Meteorology and Oceanography, *54*(2), 205-219. https://doi.org/10.3402/tellusa.v54i2.12129

Haapala, J. (2005). A numerical study of open water formation in sea ice. *Journal of Geophysical Research*, *110*(C9). https://doi.org/10.1029/2003JC002200

Hinze, J. O. (1975). Turbulence. *McGraw-Hill Book*, *2nd ed.*, New York.

Hoerner, S. F. (1965). Fluid-Dynamic Drag. Theoretical, experimental and statistical information. 5-7, 2-4 pp., *Copyright by: SF Hoerner Fluid Dynamics, Vancouver, Printed in the USA, Card Number 64-19666.*

Hunke, E. C., Lipscomb, W. H., Turner, A. K., Jeffery, N., & Elliott, S. (2013), CICE: The Los Alamos Sea Ice Model Documentation and Software User's Manual Version 5.0, *Tech. Rep.* LA-CC-06-012, Los Alamos National Laboratory, Los Alamos, N. M.

Itkin, P., Spreen, G., Cheng, B., Doble, M., Girard-Ardhuin, F., Haapala, J., Hughes, N., Kaleschke, L., Nicolaus, M. & Wilkinsonet, J. (2017). Thin ice and storms: Sea ice deformation from buoy arrays deployed during N-ICE2015. *Journal of Geophysical Research: Oceans*, *122*(6), 4661-4674. https://doi.org/10.1002/2016JC012403

Kharitonov, V. V. & Borodkin, V. A. (2020). On the results of studying ice ridges in the Shokal'skogo strait, part I: Morphology and physical parameters in-situ. *Cold Regions Science and Technology*, *174*, 103041. https://doi.org/10.1016/j.coldregions.2020.103041

Launder, B. & Spalding, D. B. (1972). Lectures in Mathematical Models of

645 Turbulence. *Academic Press*, London.

646 Leppäranta, M. & Omstedt, A. (1990). Dynamic coupling of sea ice and water for an ice
647 field with free boundaries. *Tellus A: Dynamic Meteorology and Oceanography*, *42*(4),
648 482-495. https://doi.org/10.1034/j.1600-0870.1990.t01-2-00007.x

649 Leppäranta, M. (2011). The drift of sea ice. 63, 174, 187-189, 159-160 pp., *Springer*,
650 *2nd ed.*, Berlin.

651 Lu, P., Li, Z., Cheng, B., & Leppäranta, M. (2011). A parameterization of the ice-ocean
652 drag coefficient. *Journal of Geophysical Research*, 116, C07019.
653 https://doi.org/10.1029/2010JC006878

654 Lüpkes, C., Gryanik, V. M., Hartmann, J., & Andreas, E. L. (2012). A parametrization,
655 based on sea ice morphology, of the neutral atmospheric drag coefficients for weather
656 prediction and climate models. *Journal of Geophysical Research*, *117*, D13112.
657 https://doi.org/10.1029/2012JD017630

658 Mårtensson, S., Meier, H. E. M., Pemberton, P., & Haapala, J. (2012). Ridged sea ice
659 characteristics in the Arctic from a coupled multicategory sea ice model. *Journal of*
660 *Geophysical Research*, *117*(C8). https://doi.org/10.1029/2010JC006936

661 Mai, S., Wamser, C. & Kottmeier, C. (1996). Geometric and aerodynamic roughness of
662 sea ice. *Boundary-Layer Meteorology*, 77, 233–248.
663 https://doi.org/10.1007/BF00123526

664 Martin, T., Tsamados, M., Schroeder, D., & Feltham, D. L. (2016). The impact of

variable sea ice roughness on changes in Arctic Ocean surface stress: A model study. *Journal of Geophysical Research: Oceans*, *121*(3), 1931-1952. https://doi.org/10.1002/2015JC011186

McPhee, M. G. (2002). Turbulent stress at the ice/ocean interface and bottom surface hydraulic roughness during the SHEBA drift. *Journal of Geophysical Research*, *107*(C10), SHE-11. https://doi.org/10.1029/2000JC000633

McPhee, M. G. (2012). Advances in understanding ice-ocean stress during and since AIDJEX. *Cold Regions Science and Technology*, *76-77*, 24-36. https://doi.org/10.1016/j.coldregions.2011.05.001

Obert, K. M., & Brown, T. G. (2011). Ice ridge keel characteristics and distribution in the Northumberland Strait. *Cold Regions Science and Technology*, *66*(2-3), 53-64. https://doi.org/10.1016/j.coldregions.2011.01.004

Obukhov, A. M. (1971). Turbulence in an atmosphere with a non-uniform temperature. *Boundary-Layer Meteorology*, *2*, 7–29. https://doi.org/10.1007/BF00718085

Onarheim, I. H., Eldevik, T., Smedsrud, L. H., & Stroeve, J. C. (2018). Seasonal and regional manifestation of Arctic Sea ice loss. *Journal of Climate*, *31*(12), 4917–4932. https://doi.org/10.1175/JCLI-D-17-0427.1.

Orszag, S. A., Yakhot, V., Flannery, W. S., Boysan, F., Choudhury, D., Maruzewski, J. & Patel, B. (1993). Renormalization group modeling and turbulence simulations. *International Conference on Near-Wall Turbulent Flows*, 1031-1046.

685 Overland, J. E. (1985) Atmospheric boundary layer structure and drag coefficients over
686 sea ice. *Journal of Geophysical Research*, *90*(C5), 9029-9049.
687 https://doi.org/10.1029/JC090iC05p09029

688 Petty, A. A., Tsamados, M. C., & Kurtz., N. T. (2017). Atmospheric form drag
689 coefficients over Arctic sea ice using remotely sensed ice topography data, spring
690 2009–2015. *Journal of Geophysical Research: Earth Surface*, *122*(8), 1472-1490.
691 https://doi.org/10.1002/2017JF004209

692 Pite, H. D., Topham, D. R., & van Hardenberg, B. J. (1995). Laboratory measurements
693 of the drag force on a family of two-dimensional ice keel models in a two-layer flow.
694 *Journal of Physical Oceanography*, *25*(12), 3008–3031.
695 https://doi.org/10.1175/1520-0485(1995)025<3008:LMOTDF>2.0.CO;2.

696 Rothrock, D. A., Yu, Y., & Maykut, G. A. (1999). Thinning of the Arctic sea-ice cover.
697 *Geophysical Research Letters*, *26*(23), 3469-3472.
698 https://doi.org/10.1029/1999GL010863

699 Sand, B., Bonath, V., Sudom, D. & Petrich, C. (2015). *Three Years of Measurements of*
700 *First Year Ridges in the Barents Sea and Fram Strait.* Paper presented at 23rd
701 International Conference on Port and Ocean Engineering under Arctic conditions,
702 Trondheim, Noway.

703 Schlichting, H., & Gersten, K. (2016). Boundary-layer theory. 11 pp., *Springer*, Berlin.

704 Spreen, G., Kwok, R., & Menemenlis, D. (2011). Trends in Arctic sea ice drift and role

of wind forcing: 1992–2009. *Geophysical Research Letters*, *38*, L19501. https://doi.org/10.1029/2011GL048970

Steele, M., & Boyd, T. (1998). Retreat of the cold halocline layer in the Arctic Ocean. *Journal of Geophysical Research, 103*(C5), 10419-10435.

Stroeve, J. C., Serreze, M. C., Holland, M. M., Kay, J. E., Malanik, J., & Barrett, A. P. (2012). The Arctic's rapidly shrinking sea ice cover: a research synthesis. *Climatic Change*, *110*(3-4), 1005-1027. https://doi.org/10.1007/s10584-011-0101-1

Strub-Klein, L., & Sudom, D. (2012). A comprehensive analysis of the morphology of first-year sea ice ridges. *Cold Regions Science and Technology*, *82*, 94-109. https://doi.org/10.1016/j.coldregions.2012.05.014

Timco, G. W., & Burden, R. P. (1997). An analysis of the shapes of sea ice ridges. *Cold Regions Science and Technology*, *25*(1), 65-77. https://doi.org/10.1016/S0165-232X(96)00017-1

Tsamados, M., Feltham, D. L., Schroeder, D., Flocco, D., Farrell, S. L., Kurtz, N., et al. (2014). Impact of variable atmospheric and oceanic form drag on simulations of Arctic sea ice. *Journal of Physical Oceanography*, *44*(5), 1329-1353. https://doi.org/10.1175/JPO-D-13-0215.1

Wadhams, P. & Doble, M. J. (2008). Digital terrain mapping of the underside of sea ice from a small AUV. *Geophysical Research Letters*, *35*, L01501. https://doi.org/10.1029/2007GL031921

725 Wadhams, P., Hughes, N., & Rodrigues, J. (2011). Arctic sea ice thickness
726 characteristics in winter 2004 and 2007 from submarine sonar transects. *Journal of*
727 *Geophysical Research*, *116*, C00E02. https://doi.org/10.1029/2011JC006982

728 Yakhot, V., & Orszag, S. A. (1986). Renormalization group analysis of turbulence. i.
729 basic theory. *Journal of Scientific Computing*, 1(1), 3-51.

730 Zu, Y., Lu, P., Yu, M., Cao, X., & Li, Z. (2020). Laboratory experimental study of water
731 drag force exerted on ridge keel. *Advances in Polar Science*, *31*(1): 36-42.
732 https://doi.org/10.13679/j.advps.2019.0026

733